Important Factors in the Starting Process of a Two-Dimensional Nozzle

Mitsutomo HIROTA, Tsutomu SAITO and Masahiro KAWAUCHI
Department of Aerospace System Engineering, Muroran Institute of Technology,
27-1 Mizumoto-cho Muroran-shi Hokkaido, 050-8585, JAPAN
hirota@mmm.muroran-it.ac.jp

Abstract

This paper describes an experimental and numerical simulation study of the unsteady flow of the starting process of a two-dimensional nozzle. The analysis focuses on changes in the flow-separation point, in addition to the overall flow structure. The position of the separation point in the nozzle-starting process is simulated using a turbulent model and an appropriate arrangement of the computational grid. It was found that the flow structure near the nozzle throat wall is important in the nozzle-starting process. The boundary layer including the vortical structure in this area characterizes the flow structure of the downstream side. Moreover, the aspect ratio of the computational grid should be 1:1 near the nozzle throat wall in order to reproduce the results of the nozzle-starting experiment. Furthermore, a simplified RANS turbulence model cannot reproduce the separation point in the nozzle-starting process.

1. INTRODUCTION

It is important to investigate the flow characteristics of a supersonic nozzle in order to find the causes of oscillation and to reduce the nozzle exit noise. The nozzle-starting process particularly interested us because there are unsteady flow characteristics with a shock wave, an expansion wave, a boundary layer separation, a transition to a turbulent flow, and so on. These flow characteristics mutually affect each other and become a source of oscillation and noise before long.

Shimizu and Yamanishi [1] report that side stress at the LE-7A engine nozzle used in the H-2A rocket was due to flow separation and reattachment. These flow characteristics occurred under unsteady flow and destroyed the nozzle flow symmetry. Terhardt et al. [2] indicated that there were two different modes of separation from the nozzle wall, free-shock separation (FSS) wherein the flow did not reattach downstream of separation and restricted-shock separation (RSS) wherein the flow was reattached on the nozzle wall downstream of separation. They reported that the imbalance of FSS and RSS relates to the side stress. Yonezawa et al. [3] also indicated that the LE-7A broke down during the starting process due to the side stress generated by asymmetrical flow in the transition from FSS to RSS in an unsteady flow situation. Furthermore, they demonstrated that a regenerative cooling tube was broken by the high pressure and high temperature at the nozzle wall produced by flow reattachment during the transition from RSS to FSS [4]. Based on these results, they purposely attached a step at the nozzle wall. This step controlled the separation point to reduce RSS. They [5] found that RSS occurred due to an eddy generated by a positive pressure gradient downstream of the mach disk. These results indicated that a previously generated separation point was moved through FSS or RSS [6]. Specifically, it is important to investigate the factors determining the flow-separation point to control the flow during the nozzle-starting process.

This research experimentally investigates unsteady flow characteristics during the starting of a two-dimensional nozzle. We also reproduce the observed phenomena with a numerical analysis, focusing on the separation point position. There is some relevant early research. Smith [7] presented a study of the starting process in a reflected-shock tunnel and compared the results with numerical calculations. He indicated that the secondary shock wave was in the wrong location in the steady-state model and that the structure of the flow field during the transient flow was incorrectly predicted. Amann [8] described experiment results of the flow-starting process in a wedge-like expansion nozzle compared with a rounded nozzle inlet. The numerical simulation was also done in the same

situation [9]. They indicated that the results accurately reproduced the overall experiment findings. Mouronval and Hadjadj [10] provided an overview of the phenomena involved in transient nozzle flows using Amann's configuration [8]. Some interesting research was conducted in the same period. Lee et al. [11] compared experiment results for an unsteady nozzle-starting process obtained in a shock tube with the corresponding numerical results. They reported that the overall flow structure of the experiment, from the time the primary shock wave passed through the nozzle throat to the time when the secondary shock wave was generated, was roughly consistent with that of the simulation. However, the details of the flow-like separation point were not examined. Saito and Takayama [12] reported that their experiment flow structure was roughly consistent with the corresponding numerical simulation, except for the separation point. They inferred that if the separation point in the numerical simulation were to be consistent with the experiment data, they would need further considerations, such as a turbulent model. Mouronval et al. [13] indicated that flow separation during start-up was an important characteristic. They would also need to include viscous and turbulent effects in the simulations. Therefore, this research aims at reproducing the separation point during the nozzle-starting process with a numerical simulation by introducing a turbulent model and a suitable calculation grid. The causes of any differences between the experiment and the numerical simulation [13] are also investigated. Finally, we determined that the eddy structure and the boundary layer at the nozzle throat are important factors in controlling the flow during the nozzle-starting process.

2. EXPERIMENT SETUP

Figure 1 depicts the experiment setup. A piston-drive shock tube without diaphragm is used. The total length is 7340 mm, with a rectangular cross section (150 mm × 75 mm). Pressure gauges (PCB PIEZOTRONICS: HM102A06) are installed along the shock tube. These sensors are connected to an amplifier (PCB PIEZOTRONICS: 482A22) and a scope coder (YOKOGAWA: DL-750) to measure the changing wall pressure. From these pressure samples, we determine the incident shock speed into the test section.

A two-dimensional nozzle (Fig. 2; 250 mm long, 15 mm throat width) is established at the test section where a cross-section can be observed through an optical glass window (160 mm × 280 mm).

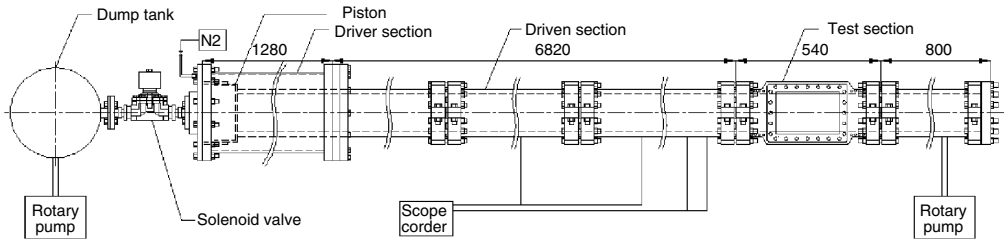

Figure 1. Schematic diagram of non-diaphragm shock tube.

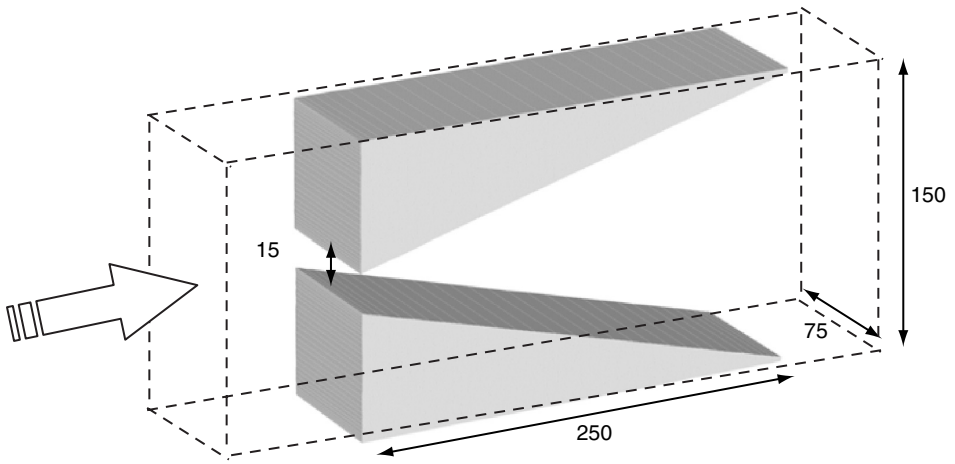

Figure 2. Schematic diagram of nozzle section.

The shock wave structure is measured with Schlieren optics. A stroboscope (SUGAWARA: ESD-VF2M-U2, 50 μ-2 ms flash time) was used as the light source for this method. A parallel ray from this source is formed with concave mirrors (MIZOJIRI: 200 mm diameter, f = 2000 mm). The signal from the pressure sensor nearest the test section is used to trigger a high-speed camera (SHIMAZU: HyperVision HPV-2) through a delay circuit in the scope coder. This system can obtain the shock-wave structure in the test section at any time. The initial pressure in the driven section was set to 10.0 kPa, and the driver section pressure was set to 35.0 kPa. These sections were filled with nitrogen gas (99.99% purity) at a temperature of 290 K. An incident shock wave with a Mach number of 1.6 was obtained with these initial conditions.

3. NUMERICAL SIMULATION METHOD

Nozzle flow is numerically simulated using a two-dimensional compressible flow solver including the equation of state for an ideal gas. The basic equations for the conservation laws of mass, momentum, and energy are expressed in differential form.

$$\mathbf{U}_t + \mathbf{F}^a_x + \mathbf{G}^a_y = 0$$

$$\mathbf{U} = \begin{bmatrix} \rho \\ \rho u \\ \rho v \\ E \end{bmatrix}, \quad \mathbf{F}^a = \begin{bmatrix} \rho u \\ \rho u^2 + p \\ \rho uv \\ u(E+p) \end{bmatrix}, \quad \mathbf{G}^a = \begin{bmatrix} \rho v \\ \rho uv \\ \rho v^2 + p \\ v(E+p) \end{bmatrix} \tag{1}$$

Here, t is time, x and y are the space coordinates, p is the pressure, ρ is the density, and u and v are the velocity components in the x and y directions. The subscripts indicate derivatives with corresponding variables. **U** is the vector of conserved variables. Vectors $\mathbf{F}^a$ and $\mathbf{G}^a$ are inviscid fluxes (a stands for advection). The total energy per unit volume E is expressed as:

$$E = \frac{p}{\gamma - 1} + \frac{1}{2}\rho\left(u^2 + v^2\right) \tag{2}$$

where g is the ratio of specific heats. Adding the effects of viscosity and heat conduction to the basic Euler equations (1) yields the following Navier-Stokes equations.

$$\mathbf{U}_t + \mathbf{F}^a_x + \mathbf{F}^d_x + \mathbf{G}^a_y - \mathbf{G}^d_y = 0$$

$$\mathbf{F}^d = \begin{bmatrix} 0 \\ \tau^{xx} \\ \tau^{xy} \\ u\tau^{xx} + v\tau^{xy} - \kappa T_x \end{bmatrix}, \quad \mathbf{G}^d = \begin{bmatrix} 0 \\ \tau^{yx} \\ \tau^{yy} \\ u\tau^{yx} + v\tau^{yy} - \kappa T_y \end{bmatrix} \tag{3}$$

Here, vectors $\mathbf{F}^d$ and $\mathbf{G}^d$ are the fluxes due to viscosity and heat conduction (d stands for diffusion). Viscosity coefficient μ is calculated from Sutherland's equation [14]. Thermal conduction coefficient κ is calculated from the equation

$$\kappa = \mu c_p / \mathrm{Pr} \tag{4}$$

where Pr is the Prantle Number (0.7) and c_p is the specific heat at constant pressure (1.039 kJ/kg·K). The basic equation is divided into an advective term and a diffusive term, and was calculated by the Operator Splitting Method. A weighted average-flux scheme (WAF) [15] is used to solve the conservation laws. The scheme is one of the higher-order extended Godunov schemes and is 2nd-order-acccurate in both time and space. It is constructed as a finite-volume method using the integral form of the basic equation. The HLLC approximate Riemann solver with a TVD-limiter function [16] is utilized

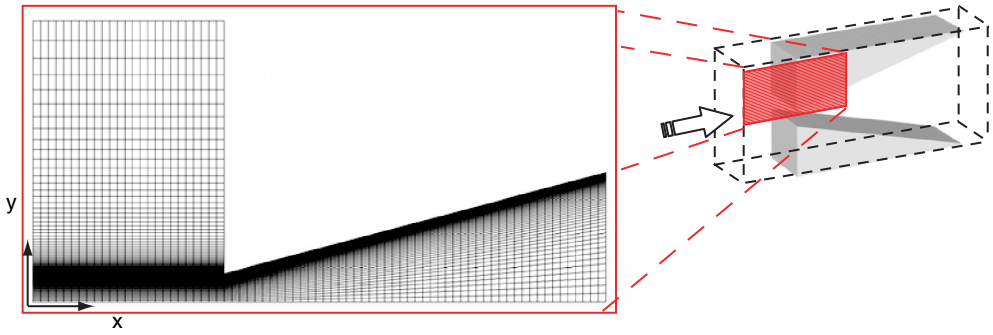

Figure 3. Computational grid image.

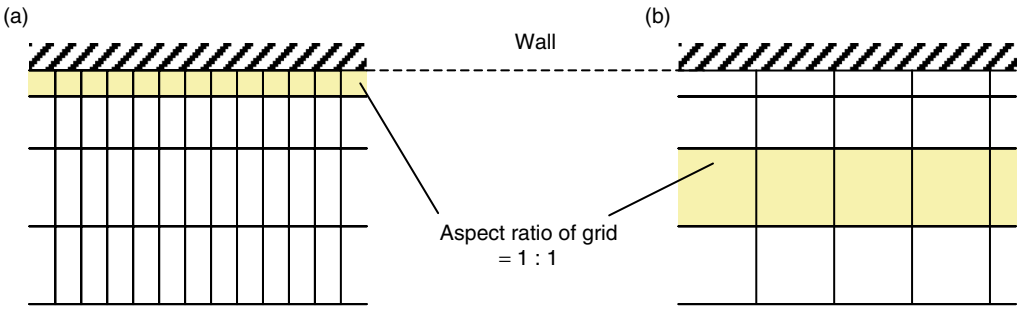

Figure 4. Conceptual diagram when the aspect ratio of the computational grid is changed.

for inter-cell flux evaluation. The Baldwin-Lomax model [17] is used as a turbulent model to consider turbulent flow.

The computational domain established from the nozzle throat to 100 mm downstream can simulate the area of the secondary shock wave observed in the downstream part after the nozzle. Figure 3 illustrates one example of the computational domain. The computational grid adopts an orthogonalization grid that does not have equal *y*-axis intervals. The number of grids in the *y* direction is unified, and the width of a minimum grid in the wall is set to 10 μm. The grid along the *x* axis is arranged at equal intervals. At this time, the aspect ratio of the computational grid is varied by changing the width of the grid along the *x* axis between 10 and 200 μm.

Figure 4 conceptually diagrams what occurs when the aspect ratio of the computational grid is changed. The minimum width of 10 μm for the grid along the *y*-axis is set at the point nearest the wall. Therefore, when the width of the calculation grid along the *x*-axis is established as 10 μm, the aspect ratio of the grid becomes 1:1 at the point nearest the wall. In this case, the grid is far from the wall (Fig. 4(a)). Moreover, a square grid (aspect ratio = 1:1) is located away from the wall surface when the width of the grid along the *x*-axis exceeds 10 μm. In this case, the upper grid is wider than the square computational grid. Conversely, the grid in the lower part is narrower than the square computational grid (Fig. 4(b)). The numerical results obtained with each grid are compared. When the square computational grid (aspect ratio = 1:1) is used, the calculation of flux is extremely accurate compared with that for a grid that collapses. We want to reproduce the experiment value by properly representing this square grid area in the boundary layer.

4. METHOD OF COMPARING NOZZLE FLOW

We compared the experiment result and the numerical result for each relevant position, namely those of the secondary shock wave, the intersection of the shock wave, and the separation point formed in the nozzle. Figure 5 is a Schlieren image that is essentially a picture of the time-series variation of the flow field in the nozzle. The time at which the shock wave reached the nozzle throat was defined as 0 sec. The incident shock wave reached the center of the nozzle throat and entered the nozzle at 15 μ sec. The incident shock wave, which does not enter the nozzle, reflects at the vertical wall and goes upstream of the duct. The diffraction wave generated in the corner of the nozzle throat spreads toward the nozzle

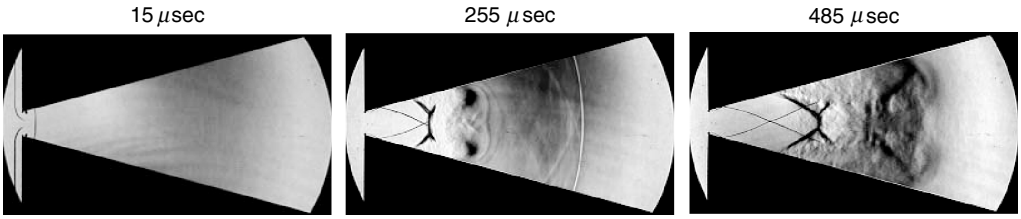

Figure 5. Schlieren images of nozzle flow changing in time.

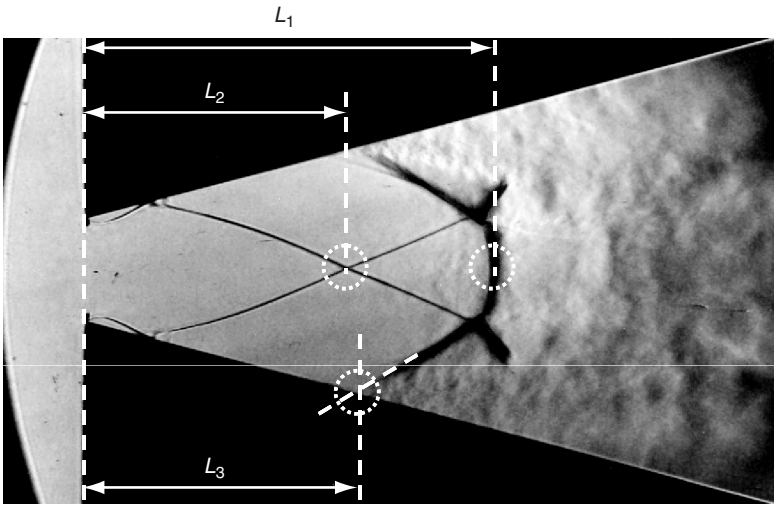

Figure 6. The definition of length of the nozzle flow characteristics.

center and reflects from the wall on the other side. The flow separates at the corner of the nozzle throat and reattaches to the nozzle wall in the downstream part. The diffraction wave and the separation flow interfere, and a secondary shock wave is formed vertically (255 μ sec). The secondary shock wave gradually moves downstream, branching off to become a λ wave because of interference with the boundary layer. One branch of the λ wave attaches to the nozzle wall, and the flow is separated (485 μ sec). The position of the secondary shock wave (L_1), the position of the intersection point of the shock wave (L_2), and the separation point of the shock wave (L_3) were measured with the passage of time (Fig. 6).

5. RESULTS AND DISCUSSION

5.1 Time change of flow structure inside nozzle

Figure 7 plots the passage of time at the secondary shock wave position (L_1). Figure7(a) is a numerical result that considers the viscosity; Fig. 7(b) is a numerical result that does not consider the viscosity. When the width of the calculation grid along the x-axis is 10 μm or 50 μm, the numerical result is comparable to the experiment value. The result with a 100 to 200 μm wide calculation grid along the x-axis is not displayed in the figure because the structure of the secondary shock wave could not be reprodced. The experiment result for the position of the secondary shock wave almost corresponds with the calculated result.

Figure 8 illustrates the time change of the intersection position of the shock wave (L_2). Figure 8(a) presents the numerical result that considers the viscosity; Fig. 8(b) presents that which does not consider the viscosity. The calculation grid width in the x-direction was varied between 10 and 200 μm, and the results were compared. The response to the change continues for 500 μsec. The result with the computational grid set at 50 μm almost corresponded to the experiment value.

Figure 9 plots the passage of time at the flow separation position (L_3). Figure 9(a) presents a numerical result that considers the viscosity; Fig. 9(b) presents that which does not consider the viscosity. The calculation grid width in the x-direction was varied between 10 and 200 μm, and the

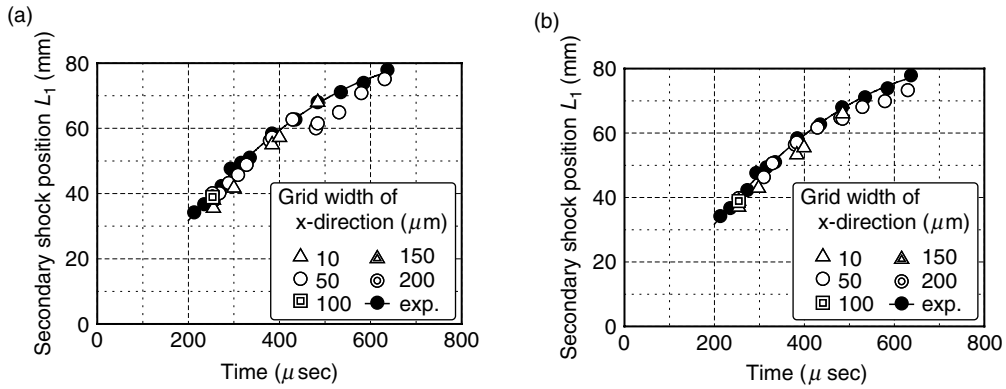

Figure 7. The influence of the grid width of x-direction on time change of a secondary shock wave position.

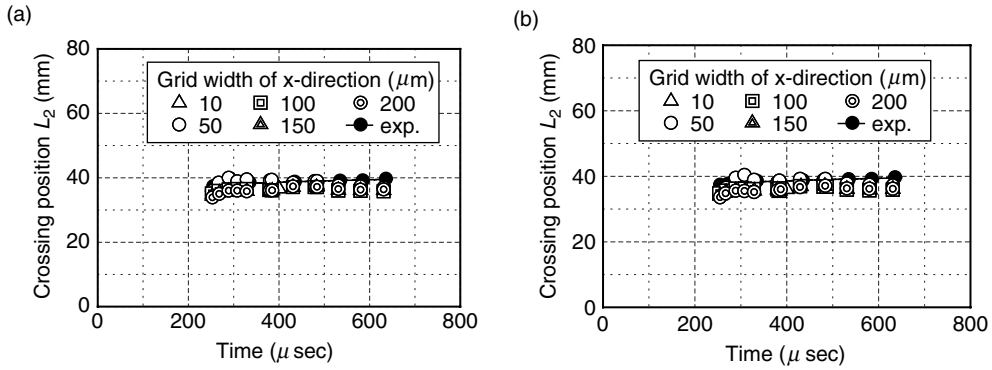

Figure 8. The influence of the grid width of x-direction on time change of a intersection position of the shock wave.

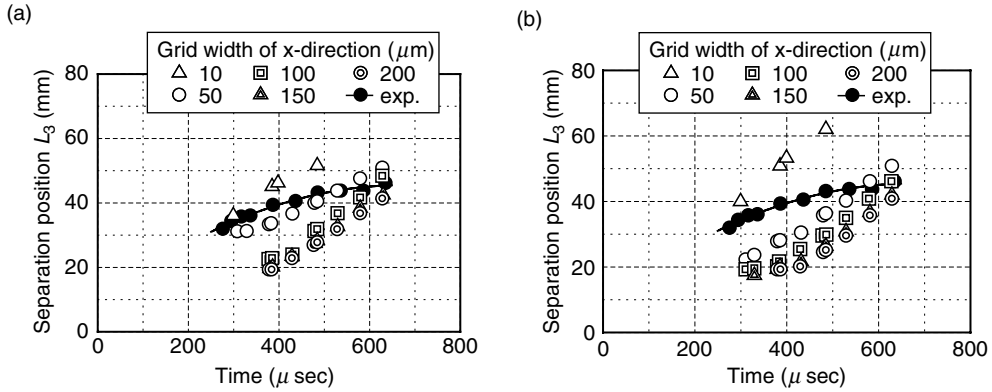

Figure 9. Transition of separation position to change in width of x direction grid.

results were compared. In Fig. 9, the change caused by the difference in the width of the computational grid in the x-direction exceeds the results of Figs. 7 and 8. When the width of the calculation grid is 100 to 200 μm, the numerical result does not correspond to the experiment result. The numerical result corresponds to the experiment result when the width of the calculation grid is 10 to 50 μm. Figure 10 plots the passage of time at the flow separation position in more detail as the position changes with the width of the computational grid in the x-direction. When the width of the computational grid in the x-direction is 27 μm (20 μm for the non-viscous computation (a)), the numerical result corresponds to the experiment result.

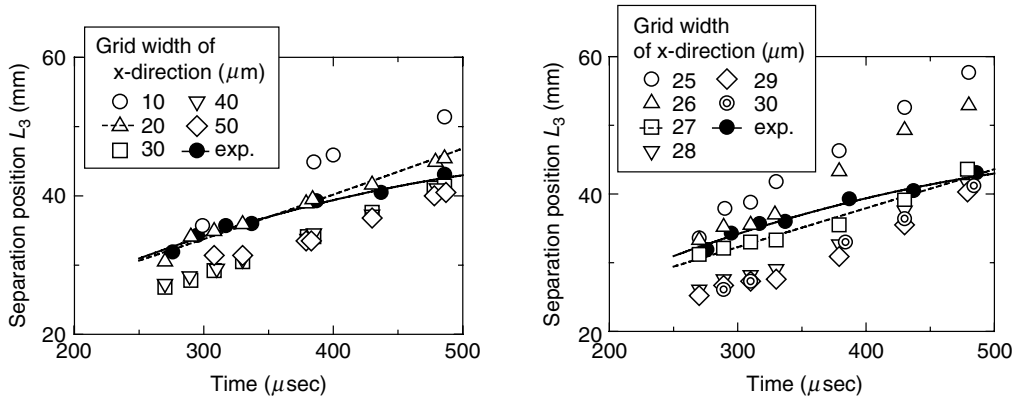

Figure 10. Transition of separation position to change in width of x direction grid (in detail).

As mentioned above, the calculation of the nozzle-starting process does not depend on the calculation grid width but roughly corresponds to the experiment (Figs. 7 and 8). However, the condition of the flow-separation point, whose experiment value does correspond to the numerical result, has been limited (Figs. 9 and 10). This tendency is similar to that seen in previous research [11–12]. An especially interesting case also reproduced the downstream separation point when non-viscous computation was done, obtaining a tendency roughly corresponding to the experiment result. In brief, flow separation is thought to be caused mainly by the non-uniformity of the speed at the nozzle entrance, not by molecular viscosity. Moreover, the larger aspect ratio of the calculation grid established a greater difference between the experiment and the calculated results. When the aspect ratio was 1:2.7 (1:2.0 for the non-viscous computation), the numerical result was able to reproduce the phenomenon. Specifically, a 1:1 grid positioned a little inside the wall can reproduce the phenomenon. It is important to provide an ideal 1:1 grid with an appropriate place and size when a physics phenomenon is reproduced with a structured grid.

5.2 Nozzle throat structure

It is necessary to provide a grid with an appropriate place and size when a numerical simulation is performed, as discussed in the foregoing paragraph for the nozzle-starting process, and to reproduce any important factors that determine flow characteristics. Here, we focus on the structure of the nozzle throat when the flow separation position of the numerical simulation corresponds to the experiment result and examine the characteristics of an important flow in the nozzle-starting process. Previous research [18–19] focused on the idea that the shock wave generated by a compression corner or a positive step separates the boundary layer that develops along the wall (Fig. 11). According to that result, the ratio (p_s/p_1) between the wall static pressure of the separation point (p_s) and the wall static pressure of the interference beginning point of the shock wave and the boundary layer (p_1) depends only on the Mach number (M_{1e}) of the main stream at the beginning point of the interference. It was determined that this pressure ratio did not depend so much on conditions downstream from the separation point such as the angle of the compression corner or the height of the step. There is a theory that assumes the pressure ratio (p_s/p_1) to be a function of M_{1e} [20]. We propose applying this theory to this free interference. In addition, Miyasato et al. [21] point out the dependence of this pressure ratio (p_s/p_1) on the Reynolds number ($Re_{\delta 1}$), based on the boundary layer thickness (δ_1) at the beginning point of the interference, not just on M_{1e}. Specifically, the separation point position will be determined by interference with the shock wave and the boundary layer. To make the separation position of the numerical simulation consistent with the experiment result, it is necessary to reproduce the interference beginning point (p_1), the structure of the boundary layer (δ_1), and the main flow velocity (M_{1e}). The present study varied the size and positioning of the computational grid near the wall and determined the condition in which the separation point corresponded with Fig. 10. Therefore, reproducing δ_1 is especially important in reproducing the separation point in the present study. The targeted nozzle does not have a smooth curve in the throat, so the flow separates in the corner of the throat, and a small vortical structure is generated. The present study focused on this structure.

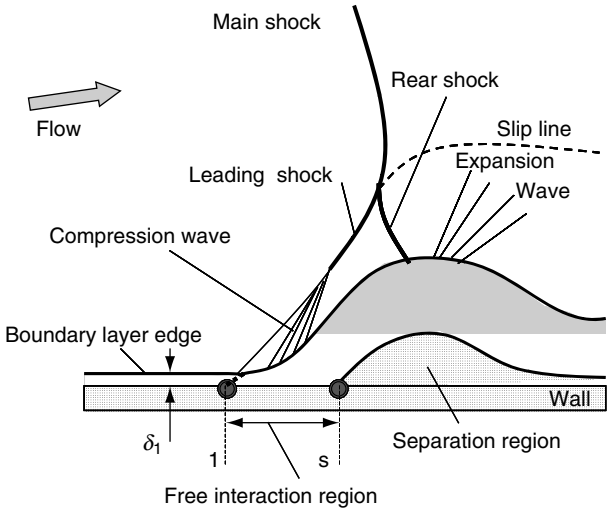

Figure 11. Diagram of free interaction at shock-induced boundary layer separation.

Figure 12 is a Schlieren image of the flow separation and reattachment near the corner of the upper part of the nozzle throat. The upper images in Fig. 12 are experiment results. We can find some vortical structures in this separation region. However, the boundary layer from this reattachment point to the separation point of the secondary shock wave seemed to be laminar because there is no clear vortical structure. The lower images in Fig. 12 are results of numerical simulation calculated with a grid that could reproduce a separation point (L_3) in the downstream flow, as seen in Fig. 10. The dotted line in the figure indicates the position at which the aspect ratio of the computational grid becomes 1:1. In this figure, the vortice structure was observed in detail near the nozzle wall. This area had almost a square computational grid. The separation boundary of the flow caused by the vortices is observed on the 1:1 line in the computational grid at 45 microseconds. The vortical structure in Fig. 12 cannot be reproduced when the computational grid that did not reproduce the separation point (L_3) is used. The results reveal the following.

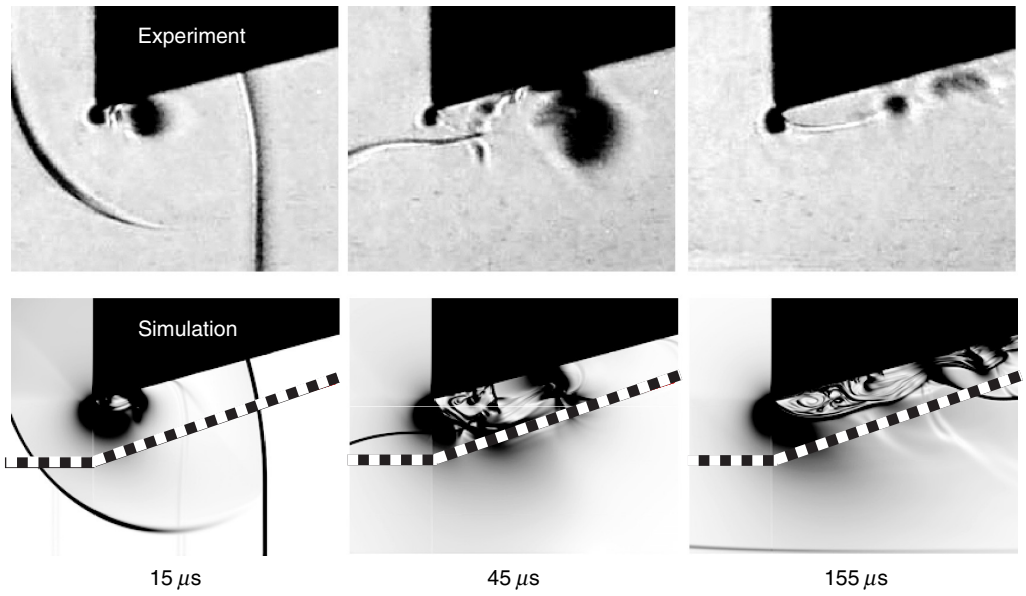

Figure 12. Comparison of nozzle entrance structures on calculation condition that separation point is corresponding to experimental result.

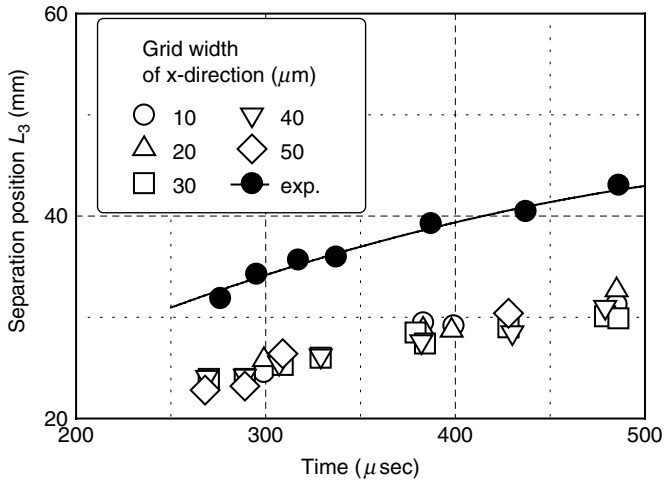

Figure 13. Transition of separation point change in width of x direction computational grid (with the turbulent model).

These vortices are generated and grow near the nozzle entrance wall, and the separation boundary extends to the main flow. Capturing the structure of this flow adequately with 1:1 computational grids is important in reproducing the down stream flow. If the structure of the flow near the nozzle entrance can be varied, the flow that develops downstream can be controlled.

The above numerical result was obtained by a laminar flow calculation that did not use the turbulent model. Reproducing the vortical structure near the wall boundary layer may be simplified by using a turbulent model, as pointed out in the previous research. The vortical structure could then be calculated similarly by using the Baldwin-Lomax turbulent model and could be compared with the experiment result. Figure 13 plots the passage of time at the separation point (L_3) when the Baldwin-Lomax turbulent model is used. In the numerical result, flow separation is observed upstream from its position in the experiment result. Moreover, the tendency and the value hardly vary, even if the aspect ratio of the computational grid is changed. The flow upstream from the secondary shock wave was observed in laminar flow, excluding the area where the flow separated at the wall. These areas will be modeled using the turbulent model.

In this case, the energy of the vortices dissipates. Therefore, the flow near the vortices of the nozzle throat could not be captured adequately. This may be why the numerical result using the turbulent model does not correspond to the experiment result. In sum, the actual phenomenon can be reproduced using a laminar-flow calculation without a turbulent model during the nozzle-starting process.

6. CONCLUSION

The starting process of a two-dimension expansion nozzle was examined. The results of an experiment using a non-diaphragm shock tube were compared with the results of a calculation that changed the aspect ratio of the computational grid. The following conclusions were obtained as a result of examining in detail the changes of the flow configuration with time.

1. The structure of the flow near the nozzle throat wall is important in the nozzle-starting process. The boundary layer, including the vortical structure in this area, characterizes the flow structure of the downstream side.
2. To reproduce the nozzle-starting process by a numerical simulation using a structured grid, the computational grid should have an aspect ratio of 1:1 near the nozzle throat wall (not the wall boundary) to simulate the vortice structures in this area.
3. A simplified RANS turbulence model cannot be used to reproduce the flow separation point in the nozzle-starting process.

ACKNOWLEDGMENTS

This work is supported by KAKENHI Grant-in-Aid for Scientific Research (C) No.21560162.

REFERENCES

[1] T. Shimizu, N. Yamanishi, "CFD in Rocket Development", *Nagare*, 24, 2005, 273–280 (in Japanese)

[2] M. Terhardt, G. Hagemann and M. Frey, "Flow separation and side-load behavior of the Vulcain engine", *AIAA Paper*, 1999–2762, 1999

[3] K. Yonezawa, Y. Watanabe, T. Morimoto, Y. Tsujimoto, K. Yokota, "Suppression of Restricted Shock Separation in Overexpanded Rocket Nozzles", *Transaction of Japan Society of Mechanical Engineers (Series B)*, 71-711, 2005, 2702–2709 (in Japanese)

[4] M. Frey, and G. Hagemann, "Restricted Shock Separation in Rocket Nozzles", *Journal of Propulsion and Power*, 16-3, 2000, 478–484

[5] K. Yonezawa, Y. Yamashita, Y. Tsujimoto, Y. Watanabe, K. Yokota, "Effect of Nozzle Contour on Flow Separation in Overexpanded Rocket Nozzle", *Transaction of Japan Society of Mechanical Engineers (Series B)*, 71-707, 2005, 1789–1797 (in Japanese)

[6] S. B. Verma, "Shock unsteadiness in a thrust optimized parabolic nozzle", *Shock Waves*, 19, 2009, 193–212

[7] C. E. Smith, "The starting process in a hypersonic nozzle", Journal of Fluid Mechanics, 24-4, 1966, 625–640

[8] H. O. Amann, "Experimental Study of the Starting Process in a Reflection Nozzle", Physics of Fluids Supplement, 12, 1969, I-150-I-153

[9] O. Igra, L. Wang, J. Falcovits, O. Amann, "Simulation of the starting flow in a wedge-like nozzle", Shock Waves, 8, 1998, 235–242

[10] A. –S. Mouronval, A. Hadjadj, "Numerical Study of the Starting Process in a Supersonic Nozzle", Journal of Propulsion and Power, 21-2, 2005, 374–377

[11] M. G. Lee, T. Murakami and M. Nishida, "Computational and Experimental Studies of Unsteady Viscous Nozzle Flows", *JSME international Journal, Series B*, 38-3, 1995, 346–352

[12] T. Saito and K. Takayama, "Numerical simulations of nozzle starting process", *Shock Waves*, 9, 1999, 73–79

[13] A. –S. Mouronval, A. Hadjadj, A. N. Kudryavtsev, D. Vandromme, "Numerical investigation of transient nozzle flow", Shock Waves, 12, 2002, 403–411

[14] D. A. Anderson, J.C. Tannehill, R. H. Pletcher, "*Computational Fluid Mechanics and Heat Transfer*", Hemisphere Publishing Corporation, New York, 1984

[15] E. F. Toro, "The Weighted Average Flux Method Applied to the Time-Dependent Euler Equations", *Phil. Trans. Roy. Soc. London*, A341, 1992, 499–530

[16] E. F. Toro, "*Riemann Solvers and Numerical Methods for Fluid Dynamics*", Springer-Verlag Berlin Heidelberg, 1997

[17] B. S. Baldwin H. Lomax, "Thin Layer Approximation and Algebraic Model for Separated Turbulent Flows", *AIAA paper*, 78–257

[18] S. M. Bogdonoff and C. E. Kepler, "Separation of a Supersonic Turbulent Boundary Layer", *Journal of the Aeronautical Sciences*, 22-6, 1955, 414–430

[19] E. E. Zukoski, "Turbulent Boundary-Layer Separation in Front of a Forward-Facing Step", *AIAA Journal*, 5-10, 1967, 1746–1753

[20] M. Arens and E. Spiegler, "Shock-Induced Boundary Layer Separation in Overexpanded Conical Exhaust Nozzles", *AIAA Journal*, 1-3, 1963, 578–581

[21] Y. Miyazato, M. Kashitani, H. D. Kim, H. Katanoda, K. Matsuo, "Shock-Induced Turbulent Boundary Layer Separation in Supersonic Nozzles", *Transaction of Japan Society of Mechanical Engineers (series B)*, 63-607, 1997, 879–886 (in Japanese)